Si/Cu-Zn(ox)/C composite as anode material for Li-ion batteries

Yawen He, Zhongbin Ye, Mohamad Chamas, Moulay Tahar Sougrati, Pierre-Emmanuel Lippens

Solid State Ionics xxx (xxxx) 115774

Contents lists available at ScienceDirect

Solid State Ionics

journal homepage: www.elsevier.com/locate/ssi

Si/Cu-Zn(ox)/C composite as anode material for Li-ion batteries

Yawen He [a, b], Zhongbin Ye [a], Mohamad Chamas [a, *], Moulay Tahar Sougrati [b], Pierre-Emmanuel Lippens [b, *]

[a] School of Chemistry and Chemical Engineering, Southwest Petroleum University, Chengdu 610500, China
[b] Institut Charles Gerhardt de Montpellier, UMR 5253 CNRS, UM, ENSCM, 34095 Montpellier cedex 5, France

ARTICLE INFO

Keywords:
Si composite
Anode
Li-ion batteries
Cu-Zn nanoparticles

ABSTRACT

The silicon based composite Si/Cu-Zn(ox)/C was prepared by ball milling from Si microparticles, Cu—Zn nanopowder heated at air and carbon black. The composite is formed by Si submicrometer particles, Cu-rich Cu_xZn, CuO, ZnO and C nanoparticles. The two oxides are electrochemically active during the first discharge, improving the nanostructuration of the composite and providing Cu nanoparticles that enhance the electronic conductivity with Cu_xZn and C. The nanostructuration helps to buffer the volume variations due to Li—Si alloying reactions during cycling. The composite is further nanostructured during the first cycles as shown by XRD and electrochemical measurements. The material was tested as anode material for Li-ion batteries, providing a reversible capacity of 800 mAh.g^{-1} during 100 cycles at current of 300 mA.g^{-1} and a good rate capability. The reversible capacity is mainly due to Li—Si alloying reactions and is stable after few cycles while the solid electrolyte interphase is stabilized after about ten cycles as shown by electrochemical impedance spectroscopy.

1. Introduction

Silicon is regarded as a promising anode material for the next generation of Li-ion batteries owing to its high theoretical specific capacity of 3580 mAh g^{-1} and its low potential vs. Li/Li^+. However, this material suffers from severe issues as its low intrinsic conductivity and large volume variations arising from Li—Si alloying reactions during the charge/discharge cycles (~300%). Such huge volume changes often lead to the pulverization and dispersion of the Si particles, the instability of the solid electrolyte interphase (SEI), the loss of electronic percolation and the electrode film delamination, which strongly reduces the electrochemical performance [1–4]. Different strategies have been proposed to address these issues, including the use of Si nanostructures [5–8], coatings and composites with carbon [9–12] and/or other materials [13–17]. Such composites generally consist of Si particles dispersed into a host matrix formed by electrochemically inactive and/or active particles. The role of the matrix is to accommodate the volume changes of the Si particles on cycling, to ensure the electronic percolation while allowing the electrolyte impregnation.

Intermetallic compounds or alloys combined with carbon as basic matrix components of Si based composite electrode materials for Li-ion batteries were recently proposed to improve the electrochemical performance. This includes Cu_3Si/Si/C [15], Ni_3Sn_4/Si/C [16] and Ni_3Sn_2-Ni_3Sn_4/Si/C [17] that can be considered as three typical composites due to their electrochemically inactive (Cu_3Si), active (Ni_3Sn_4) and mixed inactive-active (Ni_3Sn_2-Ni_3Sn_4) intermetallic matrix components. The electrochemical activity of alloying or conversion materials as matrix components increases the electrode capacity but also, and above all, improves the composite microstructure for buffering the volume variations of the Si particles during the first cycles. However, such materials also suffer from volume variations and the stability of a fully active matrix is questionable. Recently, it was shown that a mixed active-inactive Ni—Sn based matrix provides interesting electrochemical performance but it was pointed out that Sn should be partially or fully replaced by another element because of its high atomic weight and increasing price [17].

Due to its higher abundance and lower atomic weight, Zn can be considered as an interesting alternative to Sn. Zn electrochemically reacts with Li at low potential to form Li_xZn phases ending with LiZn [18]. Although Zn has a rather low specific capacity (410 mAh g^{-1}) as anode material for Li-ion batteries, it could be used as an active matrix component. Among the electrochemically inactive transition metals, Cu is a better matrix constituent than Ni to increase the electronic conductivity of the electrode material. Cu can be introduced during the synthesis of the composite material as metallic particles [19,20] or from Cu-based intermetallics such as Cu_6Sn_5 [21,22]. In the latter case, the Cu

* Corresponding authors.
E-mail addresses: mochamas@gmail.com (M. Chamas), pierre-emmanuel.lippens@umontpellier.fr (P.-E. Lippens).

https://doi.org/10.1016/j.ssi.2021.115774
Received 19 March 2021; Received in revised form 3 October 2021; Accepted 4 October 2021
0167-2738/

atoms are extruded during the first lithiation to form metallic nanoparticles. Both Cu and Zn can be found in different Cu_xZn phases as reported in the Cu—Zn binary diagram [23]. Although Zn-rich Cu—Zn alloys are electrochemically active [24], the Cu-rich compositions are not expected to react with lithium, as shown in the present paper, but provide higher electronic conductivity. In contrast, the lithiation of copper and zinc oxides, as CuO and ZnO, produces Cu and Zn nanoparticles, respectively, embedded in a Li_2O matrix [25]. Thus, combining Cu_xZn and these oxides is expected to improve the electrode nanostructuration and the conductivity during the first cycles. Such a multicomponent matrix, called here Cu-Zn(ox), is easily obtained from commercial Cu-rich Cu_xZn alloy nanopowder.

In the present work, the Si/Cu-Zn(ox)/C composite was prepared by ball-milling, that can be easily scaled up for large production of electrode materials. In addition, Si micropowder was considered to avoid the use of expensive nanoparticles that are often encountered in the preparation of Si based anode materials. Finally, carbon was added not only to enhance the electronic conductivity of the composite and the dispersion of the particles, but also to mitigate the formation of Cu_xSi phases that are electrochemically inactive [15,26]. The electrochemical mechanism of Si/Cu-Zn(ox)/C composite was investigated by combining cyclic voltammetry, galvanostatic measurements, X-ray diffraction and electrochemical impedance spectroscopy in order to determine the electrochemical behavior of the different constituents of the composite. The electrochemical performance were evaluated, showing a rather high specific capacity of 800 mAh g^{-1} at C/5 and a good rate capability with a capacity retention better than that of Si/Cu-Zn/C composites, confirming the interest of mixed intermetallic/oxide matrices.

2. Experimental

The Si/Cu-Zn/C composite was produced by ball milling of a mixture of Si microparticles (2–5 μm, 99.9% purity, Aladdin Co., Ltd), Cu—Zn alloy nanopowder (70 nm, HongWu international Co., Ltd) and carbon black (Super P, 99%, Gelon Co., Ltd). The Si/Cu-Zn(ox)/C composite was prepared in the same way except that the Cu—Zn alloy nanoparticles were replaced by Cu-Zn(ox) prepared by heating the Cu—Zn alloy nanopowder in an alumina crucible at 300 °C under atmospheric air. The 3 reactants: Cu-Zn(ox) (or Cu—Zn) (63 wt%), silicon (27 wt%) and carbon black (10 wt%) were first mixed for 5 min in an agate mortar inside a glove box. This composition was selected for a contribution of Si to the theoretical capacity of the composite of 1 Ah g^{-1}. The mixtures were transferred into a 50 mL WC pot with 8 metal balls of 1 cm diameter and a ball to mixture mass ratio of 15:1 under argon protection. They were ball milled for 48 h at 600 rpm (5 min at rest after each 10 min milling) with a planetary ball mill (TENCAN Powder Tech. Co., Ltd., XQM0.4A, rotational speed ratio of 1/2), and then stored in an Ar-filled glove box.

The crystal structure of the composites was examined by X-ray diffraction (XRD) with a X-Pert PRO MPD diffractometer by using the CuK_α radiation (λ = 0.154056 nm) and a scanning speed of 0.45° min^{-1}. The samples were protected by a Kapton film. The morphology of the particles was characterized with a field emission scanning electron microscope (SEM) FEI Inspect F50 equipped with an energy dispersive X-ray (EDX) technique for chemical analyses. The elemental analysis of the composite was also performed with focused ion beam scanning electrode microscopy (FIB-SEM) Zeiss crossbeam 540. High spatial resolution images were obtained by transmission electron microscopy (TEM) using a FEI Tecnai G2 F30 and an accelerating voltage of 300 kV. The surface of the particles was investigated by X-ray photoelectron spectroscopy (XPS) with a Thermo Fisher Scientific K-Alpha system equipped with an Al K_α X-ray source (1487 eV) under the voltage of 15 kV and a current of 10 mA. The binding energy scale was calibrated from carbon contamination by using the C 1 s peak at 284.7 eV.

The electrode material consisted of 70 wt% composite, 13 wt% sodium carboxymethyl cellulose (CMC—Na, M_w = 250,000, Aladdin Co., Ltd) and 17 wt% carbon black super P. The slurry was cast onto a Cu foil (Gelon Co., Ltd) by using a doctor blade (Gelon Co., Ltd), dried at 120 °C for 4 h under vacuum and cut into 12.7 mm diameter discs. The electrodes were incorporated into a steel coin cell (Gelon Co., Ltd., CR 2032) in Ar-filled glove box with a Li metal counter electrode and a Celgard separator (Gelon Co., Ltd., Celgard 2400). The electrolyte was prepared by dissolving 1 M $LiPF_6$ in 1:1 *v*/v ethylene carbonate (EC) and dimethyl carbonate (DMC) with 10 v.% fluoroethylene carbonate (FEC) and 2 v.% vinylene carbonate (VC) as additives. The galvanostatic charge-discharge cycles were performed at 23 °C in the range 0.05–1.2 V at different C rates (1C = 1 A g^{-1}) with a Neware BTS4000 testing system. The specific capacity is referred to the mass of the composite, which represents 70 wt% of the electrode film. The cyclic voltammetry (CV) and electrochemical impedance spectroscopy (EIS) measurements were carried out on a SP-150 electrochemical station (Biologic Ins.) with three-electrode cells as described in previous works [27,28].

3. Results and discussion

The XRD patterns of the Cu—Zn alloy nanopowder, Cu-Zn(ox) obtained after heat treatment of Cu—Zn nanopowder in air, and Si/Cu-Zn(ox)/C composite are shown in Fig. 1. The main peaks of the Cu—Zn alloy nanopowder can be assigned to body-centered cubic (BCC-B2) CuZn phase (*Pm*-3 *m*) and face-centered cubic (FCC-A1) $Cu_{0.66}Zn_{0.34}$ phase (*Fm*-3 *m*) [29,30]. Some small peaks can be attributed to Cu metal and traces of hexagonal (*P*63*mc*) ZnO. The existence of CuZn and $Cu_{0.66}Zn_{0.34}$ was expected from the product details of the supplier and confirms that Cu—Zn alloy nanopowder is a Cu-rich material. The average sizes of the $Cu_{0.66}Zn_{0.34}$ and CuZn crystalline phases, evaluated by the Scherrer's equation, are about 20 nm and 50 nm, respectively. The XRD pattern of Cu-Zn(ox) shows more peaks than Cu—Zn alloy nanopowder. Some of them can also be assigned to BCC-B2 CuZn and FCC Cu_xZn_{1-x} phases although the observed upward shift of the Bragg peaks in the latter case (~0.4°) suggests that x ≈ 0.75 instead of 0.66 [31]. The intensity of the peak at 42.7° is higher than that at 43.2°, which indicates that the Cu-rich $Cu_{0.75}Zn_{0.25}$ phase is more abundant than CuZn. The other peaks can be attributed to Cu metal and to large amounts of CuO and ZnO crystalline phases resulting from the partial oxidation of Cu—Zn nanowpowder. The average size of the particles, evaluated by the Scherrer's equation, is about 20 nm. The XRD pattern of the Si/Cu-Zn(ox)/C composite clearly shows that the ball-milling

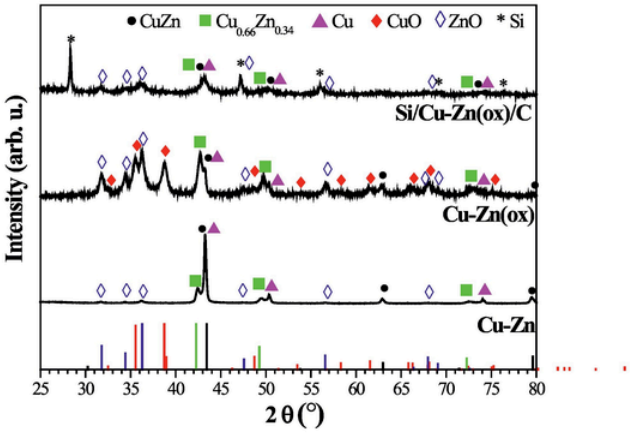

Fig. 1. XRD patterns of Cu—Zn alloy nanopowder, Cu-Zn(ox) obtained after heat treatment of Cu—Zn nanopowder in air, and Si/Cu-Zn(ox)/C composite.

process modified Cu-Zn(ox). The peaks can be assigned to Si, ZnO and Cu_xZn_{1-x} crystalline phases. The positions of the Bragg peaks of Cu_xZn_{1-x} (43.1°, 50.1°, 73.9°) are typical of FCC-A1 $Cu_{0.75}Zn_{0.25}$, as observed for Cu-Zn(ox), but the observed broadening of the peaks reflects the decrease of the particle size or variations of x around 0.75. The peaks of ZnO are rather small compared to those observed for Cu-Zn(ox), which suggests the possible amorphization or transformation of these oxides due to ball milling. The average particle sizes of the Cu_xZn_{1-x} and ZnO crystalline phases, evaluated by the Scherrer's equation, are in the range 10–15 nm. The [Cu]/[Zn] atomic ratio of the composite was evaluated to 1.9(1) by SEM-EDX and SEM-FIB. This value should be close to the [Cu]/[Zn] ratio of Cu—Zn and Cu-Zn(ox) nanopowders used for the synthesis of the composite, in line with XRD showing the existence of Cu-rich Cu_xZn phases. Only some traces of ZnO were detected in Cu—Zn pristine nanopowder, while the amounts of Cu and Zn oxides strongly increase with heat treatment in air as shown by XRD. The [O]/[Cu + Zn] atomic ratio in the composite was evaluated to 0.4(1) by SEM-EDX and SEM-FIB. This confirms the rather large amount of metal oxides in the composite formed by the oxidation of Cu—Zn nanopowder. The existence of Cu-rich Cu_xZn and Cu small particles enhances the electronic conductivity while the oxides react with lithium and change the microstructure of the composite during the first cycles.

The SEM images of the three raw materials used for the mechanosynthesis of the Si/Cu-Zn(ox)/C composite show flat plated microparticles for Si (Fig. 2a), nanoparticles of ~70 nm for carbon SP (Fig. 2b) and aggregation of nanoparticles for Cu-Zn(ox) with sizes in the range 20–100 nm (Fig. 2c). The SEM image of Si/Cu-Zn(ox)/C composite shows particle size in the range 0.1–1 μm and the size reduction of the Si particles (Fig. 2d). The SEM-EDX maps indicate that Si, Cu and Zn elements are rather homogeneously distributed among the different particles with possible particle agglomerations and decoration of the Si particles by Cu_xZn, CuO and ZnO nanoparticles (Fig. S1). The TEM images of the small particles confirm the rather good crystallinity of the Cu_xZn_{1-x} phases in contact with amorphous carbon SP (Fig. S2).

The Si 2p XPS spectrum (Fig. S3a) consists of a broad peak at 102.5 eV that can be assigned to SiO_x silicon oxides at the surface of the Si particles [32]. The Cu 2p (Fig. S3b) and Zn 2p (Fig. S3c) spectra are both formed by two peaks arising from the 1/2–3/2 spin-orbit splitting. The Cu $2p_{3/2}$ peak was fitted with two components at 932.5 eV (main contribution) and 934.2 eV that can be assigned to Cu^0 in Cu or Cu_xZn and to Cu^{2+} in CuO, respectively [22,32,33]. The binding energies of Zn^0 in Zn and Zn^{2+} in ZnO are very close and cannot be distinguished from the Zn $2p_{3/2}$ peak (1021.7 eV) [32–34]. The C 1 s peak at 284.7 eV (Fig. S3d) can be due to carbon black and hydrocarbon contamination [35].

CV measurements were performed at a sweep rate of 0.3 mV s^{-1} in the range 0.01–1.2 V (0.01–2 V for the first lithiation) to identify the electrochemical reactions in the Si/Cu-Zn(ox)/C composite (Fig. 3a). The same experiment was performed for a Si/C composite obtained with the same raw materials for comparison (Fig. 3b). The first cathodic curve of Si/Cu-Zn(ox)/C shows four reduction peaks at 1.43 V (A), 0.75 V (B), 0.3 V (C) and 0.01 V (D). The two broad structures A and B can be attributed to the degradation products of the FEC-containing electrolyte forming the solid electrolyte interphase (SEI) at the surface of the particles [36,37], as also observed for Si/C. The multistep lithiation of CuO, ending with Cu and Li_2O, could also contribute to these peaks since the proposed three-step mechanism for CuO was found in the voltage range 0.7–2 V [38,39]. The reduction peak C, not observed for Si/C, can be assigned to the transformation of ZnO into Zn and Li_2O as previously reported [40]. The lithiation of Zn is a multistep and reversible process involving different Li_xZn phases ($x \leq 1$) that are expected to contribute to the cathodic peak C [18,40,41]. The peaks A, B and C disappear in the subsequent cycles. The peak D is typical of the lithiation of crystalline Si, as observed for Si/C (Fig. 3b), and corresponds to the formation of Li_xSi amorphous phases that are progressively enriched in lithium until the formation of the $Li_{15}Si_4$ crystalline phase [42–44].There is no indication in the CV cathodic curve of the lithiation of the Cu_xZn crystalline phases detected by XRD, which suggests they are electrochemically inactive. The first anodic curve of the Si/Cu-O(ox)/C composite shows two main oxidation peaks E_1 (0.32 V) and F_1 (0.52 V) corresponding to the delithiation of Li_xSi ending with amorphous Si, as observed for the Si/C composite and reported previously [43,44]. The F_1/E_1 intensity ratio is similar for both Si/Cu-Zn(ox)/C and Si/C composites. The oxidation peaks due to the multistep

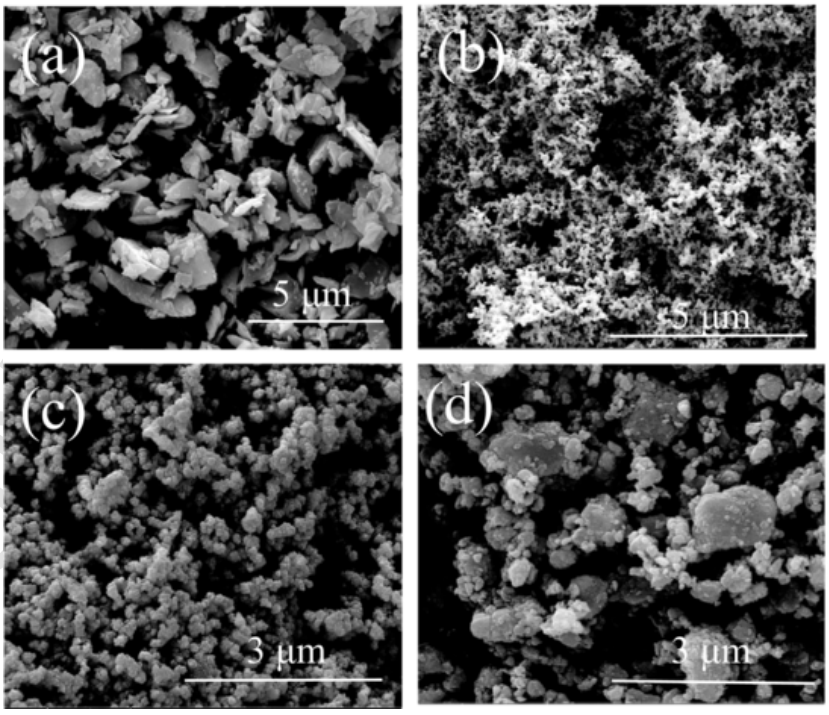

Fig. 2. SEM images of Si (a), carbon SP (b) and Cu-Zn(ox) (c) used for the ball-milling synthesis of the Si/Cu-Zn(ox)/C composite (d).

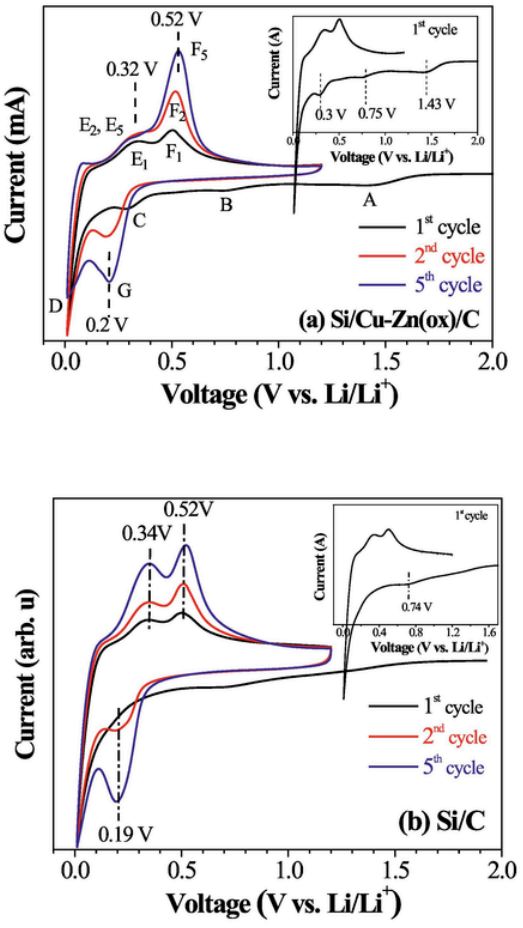

Fig. 3. CV curves for the cycles 1, 2 and 5 at a scan rate of 0.3 mV s^{-1} in the range 0.01–2 V for the composites Si/Cu-Zn(ox)/C (a) and Si/C (b).

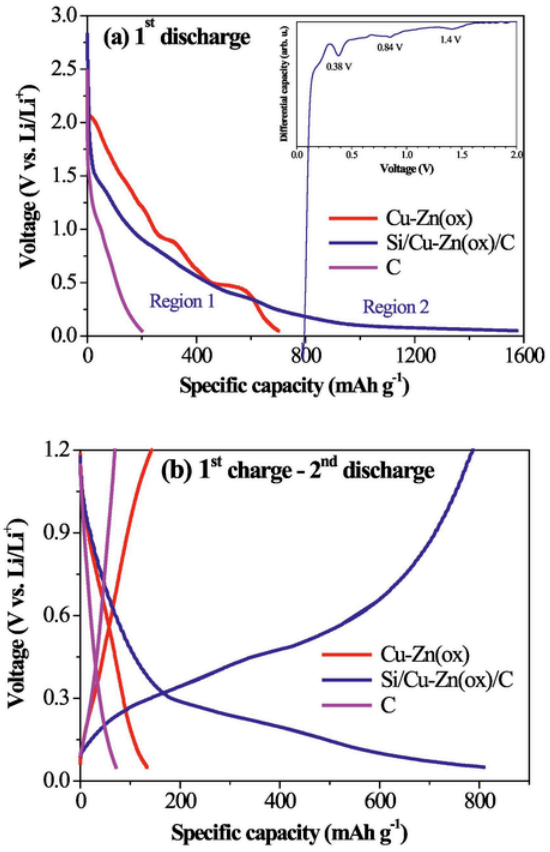

Fig. 4. Galvanostatic voltage profiles of carbon SP, Cu-Zn(ox) and Si/Cu-Zn (ox)/C: 1st discharge (a) and reversible cycle formed by the 1st charge and 2nd discharge (b). The measurements were performed in the range 0.05–1.2 V with a current density of 50 mAh g^{-1}.

delithiation of LiZn are expected in the 0.2–0.7 V range [18,40,41]. The decomposition of Li_2O occurs at voltages higher than the cutoff voltage of 1.2 V used in this work, preventing back-reactions of Zn and Cu with O and stabilizing the matrix nanostructuration [38–40,45,46]. The cathodic curves of the Si/Cu-Zn(ox)/C composite for the following cycles show two reduction peaks G (0.2 V) and D (~0 V) that are characteristic of the lithiation of amorphous Si as pristine material or occurring after the first cycle of crystalline Si [43,44,47–50]. The anodic curve of the n^{th} cycle shows two peaks E_n, F_n ($n \geq 2$) at the same positions as E_1 and F_1, respectively (Fig. 3a). They are also found in the anodic curves of Si/C (Fig. 3b) and can be attributed to the delithiation of Li_xSi. However, both peaks grow during cycling for Si/C while only the peak F_n increases significantly with n for Si/Cu-O(ox)/C. Such increase of the anodic peak during cycling reflects the gradual electrode nanostructuration as previously reported for Si [48–51]. The observed different behavior for the composite indicates that the delithiation mechanism is different, probably due to the amorphization of the Si particles or the effect of the matrix constituents as previously observed for amorphous Si and Si_xZn_{1-x} films [41,52].

The galvanostatic voltage profiles of C super P, Cu-Zn(ox) and Si/Cu-Zn(ox)/C, obtained at C/20 (50 mA g^{-1}) are compared in order to further investigate the reaction mechanisms in the composite (Fig. 4a and b). The voltage curve for the first discharge of Cu-Zn(ox) decreases from 2 to 0.05 V, showing shoulders at about 1.5 and 1.2 V, and two well-defined plateaus at 0.9 V and 0.46 V. As proposed above from the analysis of the CV measurements, the reactions above 1 V should be related to the SEI formation and the lithiation of CuO. The plateau at 0.9 V could be assigned to the reduction of Cu_2O as intermediate phase arising from the lithiation of CuO [38,39,45,53,54]. The plateau at 0.46 V is due to the transformation of ZnO into Zn and Li_2O nanoparticles [40,55,56]. The voltage curve of the Si/Cu-Zn(ox)/C composite shows a smooth decrease from 1.5 to 0.2 V for a capacity of about 800 mA g^{-1} (Region 1) and a sloping plateau until the end of discharge for an additional capacity of 800 mA g^{-1} (Region 2). The observed total capacity of the first discharge (~1600 mAh g^{-1}) is lower than the theoretical capacity of the composite (~1300 mAh g^{-1}) estimated by assuming there is no change in the relative amounts of Cu, Zn and Si due to ball milling and that about 40 at.% of Cu/Zn were transformed in CuO/ZnO during the oxidation of the Cu—Zn nanopowder. The derivative capacity vs. voltage clearly shows three peaks at about 1.4, 0.84 and 0.38 V corresponding to the CV peaks A, B and C, respectively (inset in Fig. 4a). Thus, the peaks at 0.84 and 1.4 V can be assigned to the electrolyte degradation, i.e., the reduction of EC and VC [36,37,57], or to the reduction of copper oxide. In line with the observed plateau at 0.46 V for Cu-Zn(ox), the peak at 0.38 V can be attributed to the transformation of ZnO into Zn and Li_2O. This is confirmed by the XRD pattern of the composite obtained at 0.23 V that shows small peaks at 36.2° and 38.3° attributed to hcp Zn while the peaks of ZnO, observed in the pristine material, disappeared at this voltage (Fig. 5). There are no significant changes in the XRD peaks of Si and Cu_xZn crystalline phases, confirming their electrochemical inactivity in region 1. In region 2, the voltage of Si/Cu-Zn(ox)/C is lower than 0.2 V as expected for the lithiation of Si [43,44]. This is confirmed by XRD that shows a strong decrease of the Si peak intensity from the pattern at 0.23 V to that at 0.05 V (Fig. 5). The low potential of Si in the composite during discharges could lead to the formation of lithium dendrites, which deterio-

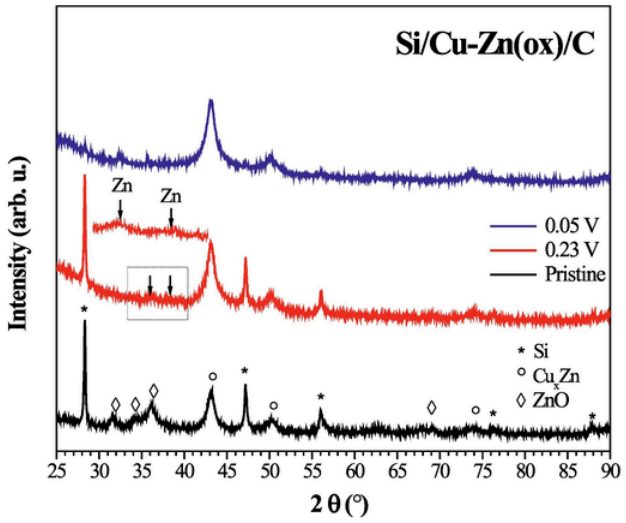

Fig. 5. XRD patterns of Si/Cu-Zn(ox)/C pristine material and lithiated electrode materials obtained at 0.2 V and 0.05 V.

rates the battery performance and could be critical for safety [58]. To overcome this problem, it was suggested to use polymer coating [59], electrolyte additives [60], polydopamide-treated [61] or metal-coated separators [62].

The experimental value of the capacity for R2 (~800 mAh·g^{-1}) is lower than the expected contribution of the 27 wt% Si to the theoretical capacity of Si/Cu-Zn(ox)/C corresponding to the formation of $Li_{15}Si_4$ (966 mAh·g^{-1}). This could be due to the voltage cutoff of 0.05 V used in the galvanostatic tests to avoid the formation of crystalline $Li_{15}Si_4$ at the end of discharge and/or the partial lithiation of Si particles. It is worth to note that the XRD peaks of the Cu_xZn crystalline phases are similar in the patterns of the pristine material, at 0.23 V and at 0.05 V, which is clear evidence of their electrochemical inactivity in the nanostructured matrix (Fig. 5).

The voltage profile of the first charge of the Si/Cu-Zn(ox)/C composite is similar to that usually reported for Si, except for a smoother increase above 0.5 V (Fig. 4b). The total capacity of the first charge is 790 mAh g^{-1}, which reflects a deep delithiation of the Li_xSi particles. The voltage profile of the second discharge differs from the first discharge and consists of a steep decrease until 0.3 V for a capacity of 180 mAh g^{-1}, followed by two pseudo-plateaus around 0.2 and 0.07 V that are typical of the two-step mechanism generally observed for the second and subsequent discharges of Si [43,44]. The voltage curves of the following charge-discharge cycles are similar to those of the first charge and second discharge, respectively. The observed capacity loss at the first cycle is mainly due to the electrolyte degradation but also to the reduction of copper and zinc oxides. In the latter case, the two conversion reactions are irreversible since the low voltage cutoff at the end of charge (1.2 V) prevents possible back reactions of Cu and Zn with O as discussed above for CV measurements.

Galvanostatic cycling performance were evaluated in the voltage range 0.05–1.2 V by considering current rates of C/20 for the first discharge and C/5 for the following charge-discharge cycles (Fig. 6a). The voltage cutoff of 0.05 V was used to avoid the formation of crystalline $Li_{15}Si_4$ at the end of discharge. The initial coulombic efficiency (ICE) of Si/Cu-Zn(ox)/C composite is of about 50% due to the SEI formation and the reduction of copper and zinc oxides. A higher ICE is obtained for Si/Cu-Zn/C (65%) that does not contain these oxides. This suggests that the SEI formation strongly contributes to the irreversible capacity loss of the first cycle. Capacity loss during the first cycles is often encountered in Si based anode materials and should be compensated by a prelithiation technique for practical applications [63]. Then, the reversible

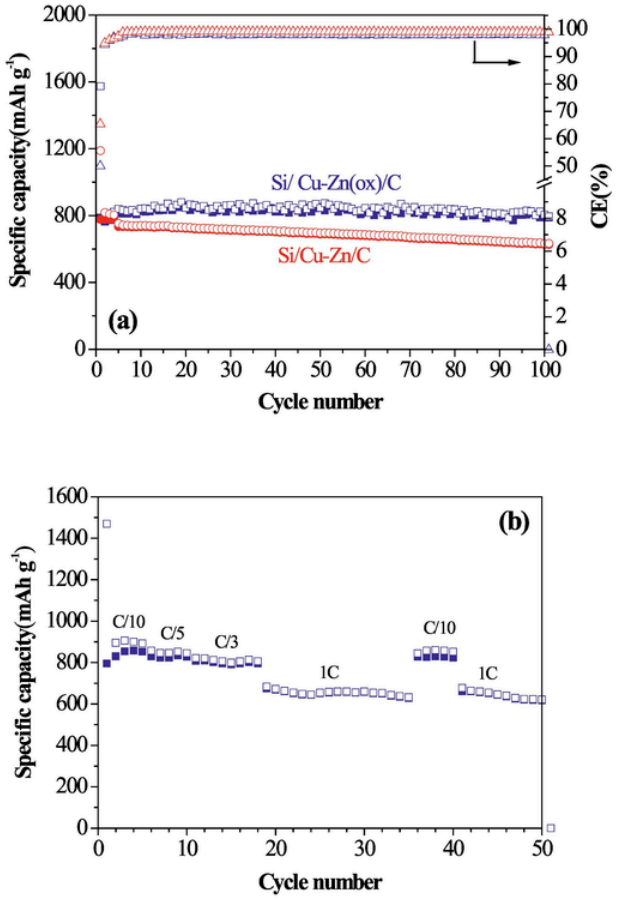

Fig. 6. Specific capacity obtained for galvanostatic discharges (open symbols) and charges (filled symbols) and coulombic efficiency (open triangles) of Si/Cu-Zn/C (red) and Si/Cu-Zn(ox)/C (blue) composites at C/5 rate (200 mAh g^{-1}) (a). Rate capability of the Si/Cu-Zn(ox)/C composite (b). (For interpretation of the references to colour in this figure legend, the reader is referred to the web version of this article.)

capacity slightly increases from 810 to 850 mAh·g^{-1} during the ten first cycles, which reflects the progressive activation of the electrode. Then, the capacity is rather stable, ending at 820 mAh g^{-1} for the 100th cycle. The coulombic efficiency of the reversible cycles increases from 94 to 98% during the ten first cycles and then keeps this value until the 100th cycle. The cycling performance of the Si/Cu-Zn/C composite is also shown for comparison. The capacity is close to that of Si/Cu-Zn(ox)/C for the first cycles and then progressively decreases until 730 mAh g^{-1} at the 100th cycle The capacity loss of more than 10% is significantly higher than that of Si/Cu-Zn(ox)/C, showing the superiority of the nanostructured Cu-Zn(ox) matrix. A comparison with previously published results on Si based anode materials is given in Table S1. The specific capacities of Si/Cu-Zn(ox)/C are 840, 830, 800 and 670 mAh g^{-1} at C/10 (100 mA g^{-1}), C/5 (200 mAh g^{-1}), C/3 (333 mAh g^{-1}) and C (1 A g^{-1}) rates, respectively, showing the good rate capability of this composite (Fig. 6b).

The evolution of the SEI layer during the first discharge-charge cycle of the Si/Cu-Zn(ox)/C composite was studied by EIS with a three-electrode Swagelok cell. The EIS measurements were performed in galvanostatic regime (C/20) at different stages of the discharge labeled D_i, where i = 1–8, and of the charge labeled C_i, where i = 1–6 (Fig. S4a). The spectra were recorded after a relaxation of 1 h at each point of measurement. Fig. S4b and S4c show the Nyquist plots of the impedance spectra during the first discharge and the first charge, respectively. The

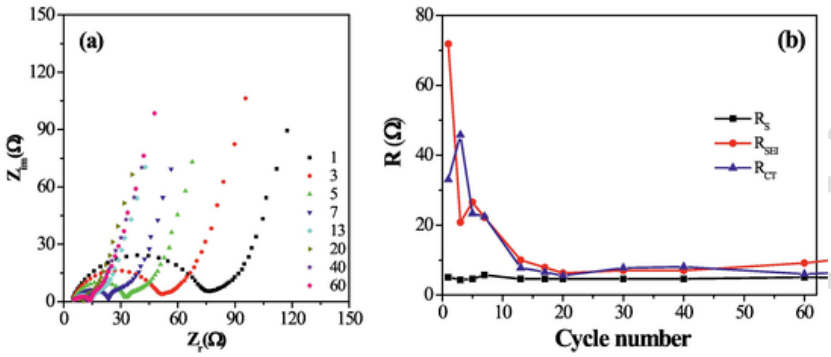

Fig. 7. EIS measurements at the end of discharges for selected cycles of Si/Cu-Zn(ox)/C: Nyquist plots (a) and variations of electrolyte resistance (R_E), solid electrolyte interphase resistance (R_{SEI}) and charge transfer resistance (R_{CT}) (b).

spectra consist of a semi-circle for both high and medium frequencies and a sloping line in the range of low frequencies. They were analyzed by the equivalent circuit $R_S(R_{SEI}Q_{SEI})(R_{CT}Q_{dl})Q$, where R_S, R_{SEI} and R_{CT} are the resistances of the electrolyte solution, SEI layer and charge transfer, respectively, while Q_{SEI}, Q_{dl} and Q are the constant phase elements of the SEI, double layer and cell geometry, respectively. The variations of R_S, R_{SEI} and R_{CT} are shown in Fig. S4d for the first cycle. The resistance of the electrolyte is constant (≈7 Ω) as usually observed. During the first discharge, the value of R_{SEI} increases from about 60 Ω (D1) to 90 Ω (D6) and is still around 80 Ω at the end of discharge (D8). This can be related to the progressive formation of the SEI due to the electrolyte degradation at the surface of the different types of particles in the composite in line with CV and galvanostatic measurements, and usually observed for Si [64]. During the charge (C_1-C_6), R_{SEI} is almost constant, suggesting there is no significant change in the thickness and the composition of the SEI, as previously reported for Si [28,64]. During the whole lithiation-delithiation process, the charge transfer resistance is almost constant, the SEI resistance shows rather small changes and the values of these two resistances are rather low, although the ICE is of about 50%. We tentatively explain such a behavior by the effect of electrolyte additives, especially FEC that has a strong effect on the properties of the SEI as discussed below, and to the enhanced conductivity of the electrode due to conductive C, Cu and Cu-rich Cu_xZn nanoparticles in the composite.

The EIS spectra were also recorded for 60 galvanostatic cycles at C/5 cycling rate (end of discharge) and fitted with the same equivalent circuit above-mentioned. The Nyquist curves show a decrease of the electrode impedance during cycling (Fig. 7a). The SEI and charge transfer resistances decrease from $R_{SEI} \approx 70$ Ω and $R_{CT} \approx 30$ Ω, respectively, to about 10 Ω after 10 cycles and then both remain constant until the end of cycling (Fig. 7b). The decrease and stabilization of the resistances with the number of cycles were previously observed for Si-based anodes and FEC-containing electrolytes in contrast to FEC-free electrolytes [65,66]. Not only the thickness, but also the composition and the morphology of the SEI are important to explain changes in EIS spectra and electrochemical performance. The SEI formed with FEC-containing electrolytes contains more inorganic species, such as Li_2CO_3 and LiF [65–67] close to the surface particles due to the degradation of FEC before that of EC and DMC with voltage decrease [68]. The SEI also contains other organic species, such as oxygen-free polymeric species [69] and polycarbonates [66,70] that stabilize the SEI and prevent the continuous degradation of the electrolyte [68]. This gives more stable, homogeneous and conductive SEI, which explains the rather low and almost constant values of the resistances after the formation process and the good capacity retention [67,68,71–73]. The SEI formation process during the ten first cycles is due to the gradual nanostructuration of electrode material. Thus, we propose that the observed trends in electrode impedance during cycling and the good capacity retention of the Si/Cu-Zn(ox)/C composite can be related to the stability of the SEI resulting from the FEC-containing electrolyte degradation, but also to the existence of conductive Cu, Cu-rich Cu_xZn and C nanoparticles.

4. Conclusion

The Si/Cu-Zn(ox)/C composite, as anode material for Li-ion batteries, was obtained by ball milling of Si microparticles, oxidized Cu—Zn nanoalloys and carbon SP. The composite consists of Si particles and a multicomponent matrix formed by Cu-rich Cu_xZn, CuO, ZnO and C nanoparticles. The nanostructured morphology of the matrix improves the electrolyte impregnation and buffers volume variations due to Li—Si alloying-dealloying reactions, while the existence of Cu-rich Cu_xZn and C nanoparticles enhances the electronic conductivity. These properties are further improved at the end of the first discharge due to the irreversible transformation of metal oxides into Li_2O and metallic nanoparticles (Cu, Zn). The electrode activation operates during several galvanostatic cycles, which improves the composite nanostructuration but also stabilizes the SEI resulting from the degradation of the FEC-containing electrolyte as shown by EIS. The Si/Cu-Zn(ox)/C composite delivers a stable specific capacity of 800 mAh g^{-1} after 100 cycles as well as good rate capability with only 20% capacity loss from 0.1 to 1 A g^{-1}.

Declaration of Competing Interest

The authors declare that they have no known competing financial interests or personal relationships that could have appeared to influence the work reported in this paper.

Acknowledgement

The authors would like to thank the National Natural Science Foundation of China grant No. 21650110463, China Scholarship Council (CSC) and Campus France PHC XU GUANGQI 2017 (38796XG) Program.

Appendix A. Supplementary data

Supplementary data to this article can be found online at https://doi.org/10.1016/j.ssi.2021.115774.

References

[1] U. Kasavajjula, C. Wang, A.J. Appleby, Nano- and bulk-silicon-based insertion anodes for lithium-ion secondary cells, J. Power Sources 163 (2007) 1003–1039, https://doi.org/10.1016/j.jpowsour.2006.09.084.
[2] X. Su, Q. Wu, J. Li, X. Xiao, A. Lott, W. Lu, B.W. Sheldon, J. Wu, Silicon-based nanomaterials for lithium-ion batteries: a review, Adv. Energy Mater. 4 (2014)

1–23, https://doi.org/10.1002/aenm.201300882.
[3] A. Casimir, H. Zhang, O. Ogoke, J.C. Amine, J. Lu, G. Wu, Silicon-based anodes for lithium-ion batteries: effectiveness of materials synthesis and electrode preparation, Nano Energy 27 (2016) 359–376, https://doi.org/10.1016/j.nanoen.2016.07.023.
[4] X. Zuo, J. Zhu, P. Müller-Buschbaum, Y.-J. Cheng, Silicon based lithium-ion battery anodes: a chronicle perspective review, Nano Energy 31 (2017) 113–143, https://doi.org/10.1016/j.nanoen.2016.11.013.
[5] X.H. Liu, L. Zhong, S. Huang, S.X. Mao, T. Zhu, J.Y. Huang, Size-dependent fracture of silicon nanoparticles during lithiation, ACS Nano 6 (2012) 1522–1531, https://doi.org/10.1021/nn204476h.
[6] X. Su, Q. Wu, J. Li, X. Xiao, A. Lott, W. Lu, B.W. Sheldon, J. Wu, Silicon-based nanomaterials for lithium-ion batteries: a review, Adv. Energy Mater. 4 (2014) 1300882, https://doi.org/10.1002/aenm.201300882.
[7] M. Gu, Y. He, J. Zheng, C. Wang, Nanoscale silicon as anode for Li-ion batteries: the fundamentals, promises, and challenges, Nano Energy 17 (2015) 366–383, https://doi.org/10.1016/j.nanoen.2015.08.025.
[8] M. Ashuri, Q. He, L.L. Shaw, Silicon as a potential anode material for Li-ion batteries: where size, geometry and structure matter, Nanoscale. 8 (2016) 74–103, https://doi.org/10.1039/c5nr05116a.
[9] F. Qu, G. She, J. Wang, X. Qi, S. Li, S. Zhang, L. Mu, W. Shi, Coating nanoparticle-assembled Si microspheres with carbon for anode material in lithium-ion battery, J. Phys. Chem. Solids 124 (2019) 312–317, https://doi.org/10.1016/j.jpcs.2018.09.037.
[10] Q. Shi, J. Zhou, S. Ullah, X. Yang, K. Tokarska, B. Trzebicka, H.Q. Ta, M.H. Rümmeli, A review of recent developments in Si/C composite materials for Li-ion batteries, Energy Storage Mater. 34 (2021) 735–754, https://doi.org/10.1016/j.ensm.2020.10.026.
[11] M. Li, X. Hou, Y. Sha, J. Wang, S. Hu, X. Liu, Z. Shao, Facile spray-drying/pyrolysis synthesis of core-shell structure graphite/silicon-porous carbon composite as a superior anode for Li-ion batteries, J. Power Sources 248 (2014) 721–728, https://doi.org/10.1016/j.jpowsour.2013.10.012.
[12] F. Dou, L. Shi, G. Chen, D. Zhang, Silicon/carbon composite anode materials for lithium-ion batteries, Electrochem. Energy Rev. 2 (2019) 149–198, https://doi.org/10.1007/s41918-018-00028-w.
[13] C. Zhu, K. Han, D. Geng, H. Ye, X. Meng, Achieving high-performance silicon anodes of lithium-ion batteries via atomic and molecular layer deposited surface coatings: an overview, Electrochim. Acta 251 (2017) 710–728, https://doi.org/10.1016/j.electacta.2017.09.036.
[14] J. Wang, T. Xu, X. Huang, H. Li, T. Ma, Recent progress of silicon composites as anode materials for secondary batteries, RSC Adv. 6 (2016) 87778–87790, https://doi.org/10.1039/C6RA08971B.
[15] S.-S. Lee, K.-H. Nam, H. Jung, C.-M. Park, Si-based composite interconnected by multiple matrices for highperformance Li-ion battery anodes, Chem. Eng. J. 381 (2020) 122619, https://doi.org/10.1016/j.cej.2019.122619.
[16] Z. Edfouf, M.T. Sougrati, C. Fariaut-Georges, F. Cuevas, J.-C. Jumas, T. Hézèque, C. Jordy, G. Caillon, M. Latroche, Reactivity assessment of lithium with the different components of novel Si/$Ni_{3.4}Sn_4$/Al/C composite anode for Li-ion batteries, J. Power Sources 238 (2013) 210–217, https://doi.org/10.1016/j.jpowsour.2013.01.197.
[17] T. Azib, N. Bibent, M. Latroche, F. Fischer, J.-C. Jumas, J. Olivier-Fourcade, C. Jordy, P.E. Lippens, F. Cuevas, Ni-Sn intermetallics as efficient buffering matrix of Si anodes in Li-ion batteries, J. Mater. Chem. A 8 (2020) 18132–18142, https://doi.org/10.1039/D0TA06047J.
[18] Y. Hwa, J.H. Sung, B. Wang, C.M. Park, H.J. Sohn, Nanostructured Zn-based composite anodes for rechargeable Li-ion batteries, J. Mater. Chem. 22 (2012) 12767–12773, https://doi.org/10.1039/c2jm31776a.
[19] P. Zuo, G. Yin, X. Hao, Z. Yang, Y. Ma, Z. Gao, Synthesis and electrochemical performance of Si/Cu and Si/Cu/graphite composite anode, Mater. Chem. Phys. 104 (2007) 444–447, https://doi.org/10.1016/j.matchemphys.2007.04.001.
[20] N. Lin, J. Zhou, J. Zhou, Y. Han, Y. Zhu, Y. Qian, Synchronous synthesis of a Si/Cu/C ternary nano-composite as an anode for Li ion batteries, J. Mater. Chem. A 3 (2015) 17544–17548, https://doi.org/10.1039/c5ta04354a.
[21] L. Fransson, E. Nordström, K. Edström, L. Häggström, J.T. Vaughey, M.M. Thackeray, Structural transformations in lithiated η'-Cu_6Sn_5 electrodes probed by in situ Mössbauer spectroscopy and X-ray diffraction, J. Electrochem. Soc. 149 (2002) A736, https://doi.org/10.1149/1.1471888.
[22] S. Naille, R. Dedryvère, H. Martinez, S. Leroy, P.E. Lippens, J.C. Jumas, D. Gonbeau, XPS study of electrode/electrolyte interfaces of η-Cu_6Sn_5 electrodes in Li-ion batteries, J. Power Sources 174 (2007) 1086–1090, https://doi.org/10.1016/j.jpowsour.2007.06.043.
[23] W. Gierlotka, S.-W. Chen, Thermodynamic descriptions of the Cu–Zn system, J. Mater. Res. 23 (2008) 258–263, https://doi.org/10.1557/JMR.2008.0035.
[24] A. Varzi, L. Mattarozzi, S. Cattarin, P. Guerriero, S. Passerini, 3D porous Cu–Zn alloys as alternative anode materials for Li-ion batteries with superior low T performance, Adv. Energy Mater. 1701706 (2017), https://doi.org/10.1002/aenm.201701706.
[25] K. Cao, T. Jin, L. Yang, L. Jiao, Recent progress in conversion reaction metal oxide anodes for Li-ion batteries, Mater. Chem. Front. 1 (2017) 2213–2242, https://doi.org/10.1039/c7qm00175d.
[26] Z. Zheng, H.H. Wu, H. Chen, Y. Cheng, Q. Zhang, Q. Xie, L. Wang, K. Zhang, M.S. Wang, D.L. Peng, X.C. Zeng, Fabrication and understanding of Cu_3Si-Si@carbon@graphene nanocomposites as high-performance anodes for lithium-ion batteries, Nanoscale 10 (2018) 22203–22214, https://doi.org/10.1039/C8NR07207H.
[27] M. Chamas, P.E. Lippens, J. Jumas, J. Hassoun, S. Panero, B. Scrosati, Electrochemical impedance characterization of $FeSn_2$ electrodes for Li-ion batteries, Electrochim. Acta 56 (2011) 6732–6736, https://doi.org/10.1016/j.electacta.2011.05.069.
[28] A. Mahmoud, M. Chamas, P.E. Lippens, Electrochemical impedance study of the solid electrolyte interphase in $MnSn_2$ based anode for Li-ion batteries, Electrochim. Acta 184 (2015) 387–391, https://doi.org/10.1016/j.electacta.2015.10.078.
[29] L.H. Beck, C.S. Smith, Copper-zinc constitution diagram, redetermined in the vicinity of the beta phase by means of quantitative metallography, J. Meteorol. (1952) 1079–1083, https://doi.org/10.1007/BF03397775.
[30] T.R. Srinivasa Rao, S. Anantharaman, Constitution of brasses below 500°C, Zeitschrift Fuer Met. 60 (1969) 312–315, https://doi.org/10.1515/ijmr-1969-600411.
[31] S.C. Ng, B.N. Brockhouse, E.D. Hallman, Characterization of large alloy single crystals by neutron diffraction, Mat.Res.Bull. 2 (1967) 69–73, https://doi.org/10.1016/0025-5408(67)90044-X.
[32] https://srdata.nist.gov/xps/selEnergyType.aspx.
[33] G. Yin, H. Abe, R. Kodiyath, S. Ueda, N. Srinivasan, A. Yamaguchi, M. Miyauchi, Selective electro- or photo-reduction of carbon dioxide to formic acid using a Cu-Zn alloy catalyst, J. Mater. Chem. A 5 (2017) 12113–12119, https://doi.org/10.1039/c7ta00353f.
[34] G. Yuan, J. Xiang, H. Jin, L. Wu, Y. Jin, Y. Zhao, Anchoring ZnO nanoparticles in nitrogen-doped graphene sheets as a high-performance anode material for lithium-ion batteries, Materials. 11 (2018) 96, https://doi.org/10.3390/ma11010096.
[35] K.K.D. Ehinon, S. Naille, R. Dedryvère, P.E. Lippens, J.C. Jumas, D. Gonbeau, Ni_3Sn_4 electrodes for Li-ion batteries: Li–Sn alloying process and electrode/electrolyte interface phenomena, Chem. Mater. 20 (2008) 5388–5398, https://doi.org/10.1021/cm8006099.
[36] B. Peng, Y. Xu, X. Wang, X. Shi, F.M. Mulder, The electrochemical performance of super P carbon black in reversible Li/Na ion uptake, Sci. China Phys. Mech. Astron. 60 (2017), https://doi.org/10.1007/s11433-017-9022-y.
[37] T. Jaumann, J. Balach, M. Klose, S. Oswald, U. Langklotz, A. Michaelis, J. Eckert, L. Giebeler, SEI-component formation on sub 5 nm sized silicon nanoparticles in Li-ion batteries: the role of electrode preparation FEC addition and binders, Phys. Chem. Chem. Phys. 17 (2015) 24956–24967, https://doi.org/10.1039/C5CP03672K.
[38] A. Débart, L. Dupont, P. Poizot, J.-B. Leriche, J.M. Tarascon, Transmission electron microscopy study of the reactivity mechanism of tailor-made CuO particles toward lithium, J. Electrochem. Soc. 148 (2001) A1266–A1274, https://doi.org/10.1149/1.1409971.
[39] K. Chen, D. Xue, S. Komarneni, Beyond theoretical capacity in cu-based integrated anode: insight into the structural evolution of CuO, J. Power Sources 275 (2015) 136–143, https://doi.org/10.1016/j.jpowsour.2014.11.002.
[40] X. Shen, D. Mu, S. Chen, B. Wu, F. Wu, Enhanced electrochemical performance of ZnO-loaded/porous carbon composite as anode materials for lithium ion batteries, ACS Appl. Mater. Interfaces 5 (2013) 3118–3125, https://doi.org/10.1021/am400020n.
[41] T.D. Hatchard, M.N. Obrovac, J.R. Dahn, Electrochemical reaction of the $Si_{1-x}Zn_x$ binary system with Li, J. Electrochem. Soc. 152 (2005) A2335, https://doi.org/10.1149/1.2098407.
[42] S. Misra, N. Liu, J. Nelson, S.S. Hong, Y. Cui, M.F. Toney, In situ X-ray diffraction studies of (de)lithiation mechanism in silicon nanowire anodes, ACS Nano 6 (2012) 5465–5473, https://doi.org/10.1021/nn301339g.
[43] M.N. Obrovac, L.J. Krause, Reversible cycling of crystalline silicon powder, J. Electrochem. Soc. 154 (2007) 103–108, https://doi.org/10.1149/1.2402112.
[44] J. Li, J.R. Dahn, An in situ X-Ray diffraction study of the reaction of Li with crystalline Si, J. Electrochem. Soc. 154 (2007) A156, https://doi.org/10.1149/1.2409862.
[45] S. Grugeon, S. Laruelle, R. Herrera-Urbina, L. Dupont, P. Poizot, J.M. Tarascon, Particle size effects on the electrochemical performance of copper oxides toward lithium, J. Electrochem. Soc. 148 (2001) A285–A292, https://doi.org/10.1149/1.1353566.
[46] Z.-W. Fu, F. Huang, Y. Zhang, Y. Chu, Q.-Z. Qin, The electrochemical reaction of zinc oxide thin films with lithium, J. Electrochem. Soc. 150 (2003) A714, https://doi.org/10.1149/1.1570410.
[47] T.D. Hatchard, J.R. Dahn, In Situ XRD and electrochemical study of the reaction of lithium with amorphous silicon, J. Electrochem. Soc. 151 (2004) A838–A842, https://doi.org/10.1149/1.1739217.
[48] Y. Xu, G. Yin, Y. Ma, P. Zuo, X. Cheng, Nanosized core/shell silicon@carbon anode material for lithium ion batteries with polyvinylidene fluoride as carbon source, J. Mater. Chem. 20 (2010) 3216–3220, https://doi.org/10.1039/b921979j.
[49] R. Hu, W. Sun, Y. Chen, M. Zeng, M. Zhu, Silicon/graphene based nanocomposite anode: large-scale production and stable high capacity for lithium ion batteries, J. Mater. Chem. A 2 (2014) 9118–9125, https://doi.org/10.1039/c4ta01013b.
[50] Y.X. Yin, S. Xin, L.J. Wan, C.J. Li, Y.G. Guo, Electrospray synthesis of silicon/carbon nanoporous microspheres as improved anode materials for lithium-ion batteries, J. Phys. Chem. C 115 (2011) 14148–14154, https://doi.org/10.1021/jp204653y.
[51] M. Green, E. Fielder, B. Scrosati, M. Wachtler, J. Serra Moreno, Structured silicon anodes for lithium battery applications, Electrochem. Solid-State Lett. 6 (2003) A75–A79, https://doi.org/10.1149/1.1563094.
[52] T.D. Hatchard, M.N. Obrovac, J.R. Dahn, A comparison of the reactions of the SiSn, SiAg, and SiZn binary systems with Li, J. Electrochem. Soc. 153 (2006) A282–A287, https://doi.org/10.1149/1.2140607.
[53] C. Wang, D. Higgins, F. Wang, D. Li, R. Liu, G. Xia, N. Li, Q. Li, H. Xu, G. Wu, Controlled synthesis of micro/nanostructured CuO anodes for lithium-ion batteries, Nano Energy 9 (2014) 334–344, https://doi.org/10.1016/j.nanoen.2014.08.009.
[54] X. Hu, C. Li, X. Lou, Q. Yang, B. Hu, Hierarchical CuO octahedra inherited from copper metal-organic frameworks: high-rate and high-capacity lithium-ion storage

materials stimulated by pseudocapacitance, J. Mater. Chem. A 5 (2017) 12828–12837, https://doi.org/10.1039/c7ta02953e.
[55] F. Li, L. Yang, G. Xu, H. Xiaoqiang, X. Yang, X. Wei, Z. Ren, G. Shen, G. Han, Hydrothermal self-assembly of hierarchical flower-like ZnO nanospheres with nanosheets and their application in Li-ion batteries, J. Alloys Compd. 577 (2013) 663–668, https://doi.org/10.1016/j.jallcom.2013.06.147.
[56] X.H. Huanga, X.H. Xiab, Y.F. Yuanc, F. Zhoua, Porous ZnO nanosheets grown on copper substrates as anodes for lithium ion batteries, Electrochim. Acta 56 (2011) 4960–4965, https://doi.org/10.1016/j.electacta.2011.03.129.
[57] T. Jaumann, J. Balach, U. Langklotz, V. Sauchuk, M. Fritsch, A. Michaelis, V. Teltevskij, D. Mikhailova, S. Oswald, M. Klose, G. Stephani, R. Hauser, J. Eckert, L. Giebeler, Lifetime vs. rate capability: understanding the role of FEC and VC in high-energy Li-ion batteries with nano-silicon anodes, Energy Storage Mater. 6 (2017) 26–35, https://doi.org/10.1016/j.ensm.2016.08.002.
[58] L.A. Selis, J.M. Seminario, Dendrite formation in silicon anodes of lithium-ion batteries, RSC Adv. 8 (2018) 5255–5267, https://doi.org/10.1039/C7RA12690E.
[59] J. Luo, C.E. Wu, L.Y. Su, S.S. Huang, C.C. Fang, Y.S. Wu, J. Chou, N.L. Wu, A proof-of-concept graphite anode with a lithium dendrite suppressing polymer coating, J. Power Sources 406 (2018) 63–69, https://doi.org/10.1016/j.jpowsour.2018.10.002.
[60] X.Q. Zhang, X.-B. Cheng, X. Chen, C. Yan, Q. Zhang, Fluoroethylene carbonate additives to render uniform Li deposits in lithium metal batteries, Adv. Funct. Mater. 1605989 (2017), https://doi.org/10.1002/adfm.201605989.
[61] M.L. Zhou, Z. Zhang, J. Xu, J. Wei, J. Yu, Z.Y. Yang, PDA modified commercial paper separator engineering with excellent lithiophilicity and mechanical strength for lithium metal batteries, J. Electroanal. Chem. 868 (2020) 114195, https://doi.org/10.1016/j.jelechem.2020.114195.
[62] H. Lee, X. Ren, C. Niu, L. Yu, M.H. Engelhard, I. Cho, M.H. Ryou, H. Soo Jin, H.T. Kim, J. Liu, W. Xu, J.G. Zhang, Suppressing lithium dendrite growth by metallic coating on a separator, Adv. Funct. Mater. 1704391 (2017), https://doi.org/10.1002/adfm.201704391.
[63] F. Holtstiege, P. Bärmann, R. Nölle, M. Winter, T. Placke, Pre-lithiation strategies for rechargeable energy storage technologies: concepts, promises and challenges, Batteries 4 (2018) 4, https://doi.org/10.3390/batteries4010004.
[64] B. Philippe, R. Dedryvère, J. Allouche, F. Lindgren, M. Gorgoi, H. Rensmo, D. Gonbeau, K. Edström, Nanosilicon electrodes for lithium-ion batteries: interfacial mechanisms studied by hard and soft X-ray photoelectron spectroscopy, Chem. Mater. 24 (2012) 1107–1115, https://doi.org/10.1021/cm2034195.
[65] C.C. Nguyen, B.L. Lucht, Comparative study of fluoroethylene carbonate and vinylene carbonate for silicon anodes in lithium ion batteries, J. Electrochem. Soc. 161 (2014) A1933–A1938, https://doi.org/10.1149/2.0731412jes.
[66] W.J. Tang, W.J. Peng, G.C. Yan, H.J. Guo, X.H. Li, Y. Zhou, Effect of fluoroethylene carbonate as an electrolyte additive on the cycle performance of silicon-carbon composite anode in lithium-ion battery, Ionics 23 (2017) 3281–3288, https://doi.org/10.1007/s11581-017-2143-5.
[67] K. Schroder, J. Alvarado, T.A. Yersak, J. Li, N. Dudney, L.J. Webb, Y.S. Meng, K.J. Stevenson, The effect of fluoroethylene carbonate as an additive on the solid electrolyte interphase on silicon lithium-ion electrodes, Chem. Mater. 27 (2015) 5531–5542, https://doi.org/10.1021/acs.chemmater.5b01627.
[68] C. Xu, F. Lindgren, B. Philippe, M. Gorgoi, F. Björefors, K. Edström, T. Gustafsson, Improved performance of the silicon anode for Li-ion batteries: understanding the surface modification mechanism of fluoroethylene carbonate as an effective electrolyte additive, Chem. Mater. 27 (2015) 2591–2599, https://doi.org/10.1021/acs.chemmater.5b00339.
[69] E. Markevich, G. Salitra, D. Aurbach, Fluoroethylene carbonate as an important component for the formation of an effective solid electrolyte interphase on anodes and cathodes for advanced Li-ion batteries, ACS Energy Letters 2 (2017) 1337–1345, https://doi.org/10.1021/acsenergylett.7b00163.
[70] J. Kim, O.B. Chae, B.L. Lucht, Structure and stability of the solid electrolyte interphase on silicon anodes of lithium-ion batteries, J. Electrochem. Soc. 168 (2021) 030521, https://doi.org/10.1149/1945-7111/abe984.
[71] W. Wang, S. Yang, Enhanced overall electrochemical performance of silicon/carbon anode for lithium-ion batteries using fluoroethylene carbonate as an electrolyte additive, J. Alloys Compd. 695 (2017) 3249–3255, https://doi.org/10.1016/j.jallcom.2016.11.248.
[72] Y. Jin, N.J.H. Kneusels, L.E. Marbella, E. Castillo-Martínez, P.C.M.M. Magusin, R.S. Weatherup, E. Jónsson, T. Liu, S. Paul, C.P. Grey, Understanding fluoroethylene carbonate and vinylene carbonate based electrolytes for Si anodes in lithium ion batteries with NMR spectroscopy, J. Am. Chem. Soc. 140 (2018) 9854–9867, https://doi.org/10.1021/jacs.8b03408.
[73] Y.B. Yohannes, S.D. Lin, N.-L. Wu, In situ DRIFTS analysis of solid electrolyte interphase of Si-based anode with and without fluoroethylene carbonate additive, J. Electrochem. Soc. 164 (2017) A3641–A3648, https://doi.org/10.1149/2.0681714jes.